

pubs.acs.org/NanoLett Letter

# Spatial Interactions in Hydrogenated Perovskite Nickelate Synaptic Networks

Ravindra Singh Bisht,\* Jaeseoung Park, Haoming Yu, Chen Wu, Nikhil Tilak, Sylvie Rangan, Tae J. Park, Yifan Yuan, Sarmistha Das, Uday Goteti, Hee Taek Yi, Hussein Hijazi, Abdullah Al-Mahboob, Jerzy T. Sadowski, Hua Zhou, Seongshik Oh, Eva Y. Andrei, Monica T. Allen, Duygu Kuzum, Alex Frano, Robert C. Dynes, and Shriram Ramanathan\*



Cite This: Nano Lett. 2023, 23, 7166-7173



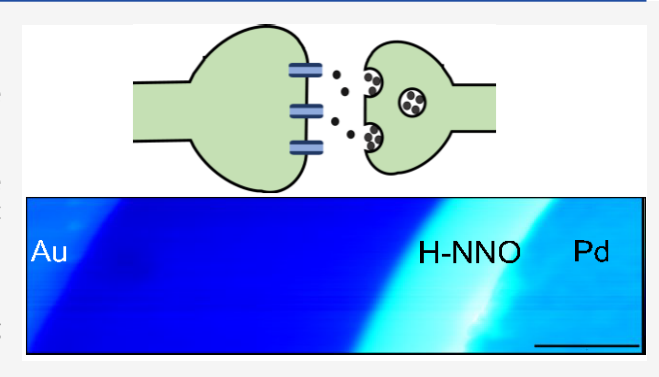
ACCESS

III Metrics & More

Article Recommendations

Supporting Information

ABSTRACT: A key aspect of how the brain learns and enables decision-making processes is through synaptic interactions. Electrical transmission and communication in a network of synapses are modulated by extracellular fields generated by ionic chemical gradients. Emulating such spatial interactions in synthetic networks can be of potential use for neuromorphic learning and the hardware implementation of artificial intelligence. Here, we demonstrate that in a network of hydrogen-doped perovskite nickelate devices, electric bias across a single junction can tune the coupling strength between the neighboring cells. Electrical transport measurements and spatially resolved diffraction and nanoprobe X-ray and scanning microwave impedance spectroscopic studies suggest that graded proton distribution in the inhomogeneous medium of hydrogen-



doped nickelate film enables this behavior. We further demonstrate signal integration through the coupling of various junctions.

KEYWORDS: neuromorphic computing, perovskite nickelates, synaptic plasticity, quantum materials

principal goal of research in the field of neuromorphic computing is to emulate aspects of biological intelligence in hardware. Synapses in the brain are responsible for memory, learning, and in a broader sense control of the functioning of neural circuits. This is accomplished in part by the ability of the synapses to modify their weight (termed plasticity), thereby modulating the firing of neuronal action potentials. Recent neuroscience studies have demonstrated synapses to be crucial for neural network regulation beyond simple plasticity.<sup>2</sup> In fact, the dynamic state of synapses has been noted as crucial for neural computation besides serving as memory storage.<sup>3</sup> Synapses can control the flow of information either via chemical, electrical, or even a combination of both mechanisms (mixed synapses) as noted in studies on teleost fish.<sup>4</sup> Extracellular fields generated by the ionic chemical potential gradients may enable synapses to control signal transmission in small-scale networks.<sup>5</sup> That is the coupling of neighboring neuronal cells can be profoundly modified by individual synaptic action due to the local chemical disturbances occurring over characteristic neurotransmitter diffusional length scales, thereby affecting signal transmission in a neural circuit. It has been suggested that such coupling is important for establishing network function and complex spatiotemporal patterns of local field potentials in neuronal ensembles in various length scales. 6-9 Gamma band activity and sharp-wave

features are important for perception, learning, and memory in the brain. 10-13 Function in large-scale neural networks requires changes and control of membrane potentials of individual neurons which is achieved by integration of incoming signals from a large number of neurons. Furthermore, neural networks such as those based on the Ising model 4 shows that emergent computational phenomena such as categorization and associative memory 15,16 are a consequence of interactions between network elements with wide-ranging spatial and temporal scales. Emulating the subtleties and complexity seen in various biological neural networks into artificial intelligence represents a frontier problem. 17

Hydrogen donor doping of nickelates (e.g.,  $NdNiO_3(NNO)$ ) has been shown to result in several orders of magnitude changes in electrical resistance at room temperature resulting from an  $e_g^2$  half-filled configuration of the Ni dorbitals upon electron injection. <sup>18</sup> The magnitude of resistance

Received: June 5, 2023 Revised: July 17, 2023 Published: July 28, 2023





Nano Letters pubs.acs.org/NanoLett Letter

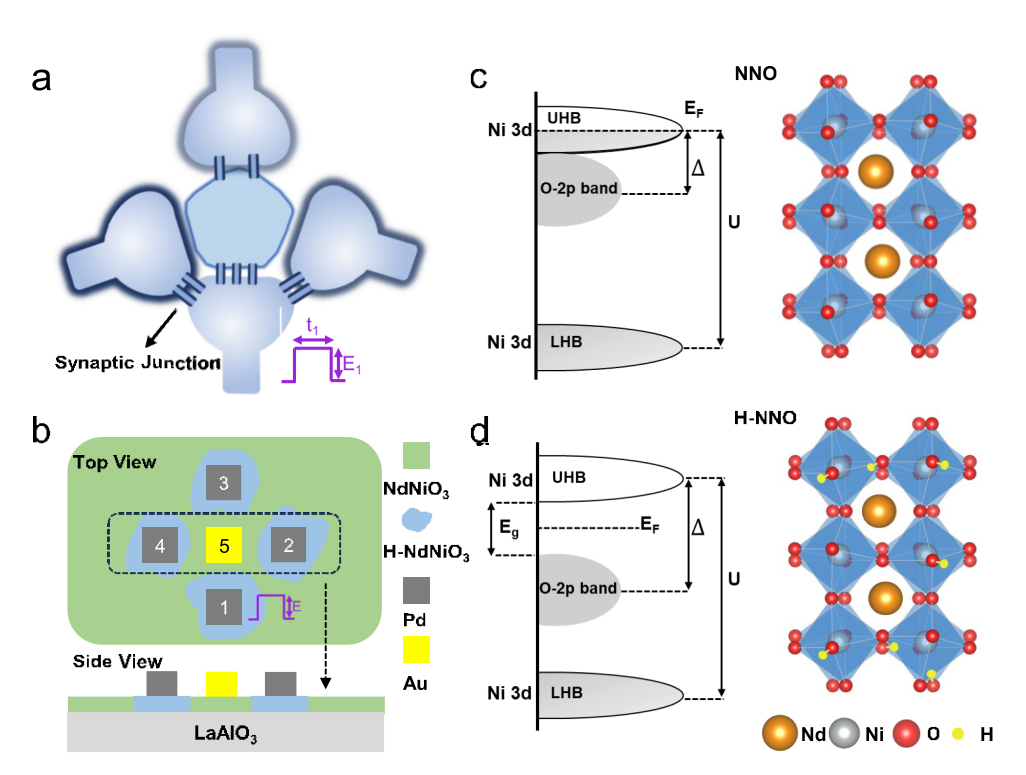


Figure 1. Schematic illustration of coupling between neuronal cells and electronic analogue in NdNiO<sub>3</sub>. (a) Extracellular field coupling among different neuronal cells in a biological synaptic network. The coupling between neighboring cells can be tuned by synaptic action across one junction. The different shades of color illustrate different coupling strengths. Each cell represents a neuron and the lines connecting the cells represent synaptic junction. (b) Schematic (top and cross-sectional view) of the in-plane NNO device with Pd and Au electrodes. The Pd electrodes serve as a catalyst for hydrogen doping of the NNO film with heavier doping proximal to the Pd electrode. The graded concentration of the dopants across the electrode junctions can be modulated by electric bias. The synaptic action across electrode 1 leads to a change in the coupling strength with nearby electrodes. The heavily doped region is shown in blue color as a visual guide. (c) Schematic of band diagram and structure of perovskite NNO at room temperature. (d) Hydrogen doping leads to a reduction in Ni valence from +3 to +2 and as a result of electronic correlation, a bandgap opens up. The protons diffused in the NNO lattice are weakly coupled to the oxygen atom of Ni–O octahedra. *E*, *E*<sub>F</sub>, *U*, and a represent the electronic bandgap, Fermi energy, on-site coulomb repulsion, and charge transfer energy, respectively.

change in a device can be controlled over several orders of magnitude by partial doping of the material utilizing forming gas annealing time-temperature envelopes. Protons reside in interstitial sites and can drift under electric fields. The extreme sensitivity of the electrical resistance of the nickelate to the concentration and distribution of protons in the lattice enables a wide range of resistance states that can be realized under pulsed voltage bias. 19,20 Tuning resistance in individual hydrogen-doped nickelate devices under electric fields has been demonstrated previously; however, understanding its impact in local networks is largely unknown. Here, we show that while potentiation, depression, and learning rates of an individual synaptic device can be systematically controlled by pulsed fields, the resistance of adjacent gap junctions can also be simultaneously modified due to the spatial drift of the protons. An electronically inhomogeneous medium comprising spatially varying proton concentrations enables this coupling and is verified by multimodal scanning probe techniques (e.g., scattering and spectroscopy). At the same time, resistance tuning is limited to proximal nickelate junctions and hence is promising to realize an artificial neurological substrate for brain-inspired electronics. Utilizing arrays of hydrogen-doped nickelate (H-NNO) devices, we then demonstrate signal integration through various junctions an operation important for the integration of incoming signals that enable the function of neural networks.

The synaptic junction is the space between two neuronal cells, which controls electrical transmission/communication. The strengthening (potentiation) and weakening (depression) of the synaptic weight depend on the magnitude of the stimulus. The coupling between the different neuronal cells is depicted in Figure 1a. As shown, the stimulus applied to a single cell results in changing the coupling among the cells (shaded region with different gradients). In Figure 1b, we show the schematic (top and cross-sectional view) of the analogous H-NNO device study to illustrate the aforementioned concept. Each electrode represents a neuron node, and the region between two electrodes represents a synapse. Figure 1c shows the band diagram of metallic NNO film at room temperature.<sup>21–23</sup> The hydrogen donor doping in the NNO leads to a change in the nominal nickel valence state from +3 to +2 due to electron filling in e gorbitals and opens an electronic bandgap as schematically shown in Figure 1d. The protons upon hydrogenation couple weakly to the oxygen (Figure 1d) of the NNO lattice.<sup>24</sup> The ability to vary the spatial distribution of the protons and hence channel resistance under an electric field is utilized for neuromorphic functionality.

In Figure 2a, the *I–V* characteristics of pristine NNO and H-NNO films are shown. As depicted, the resistance of H-NNO is greater than that of the NNO film (see Figure S1 and the Supporting Information for film growth, device fabrication, and

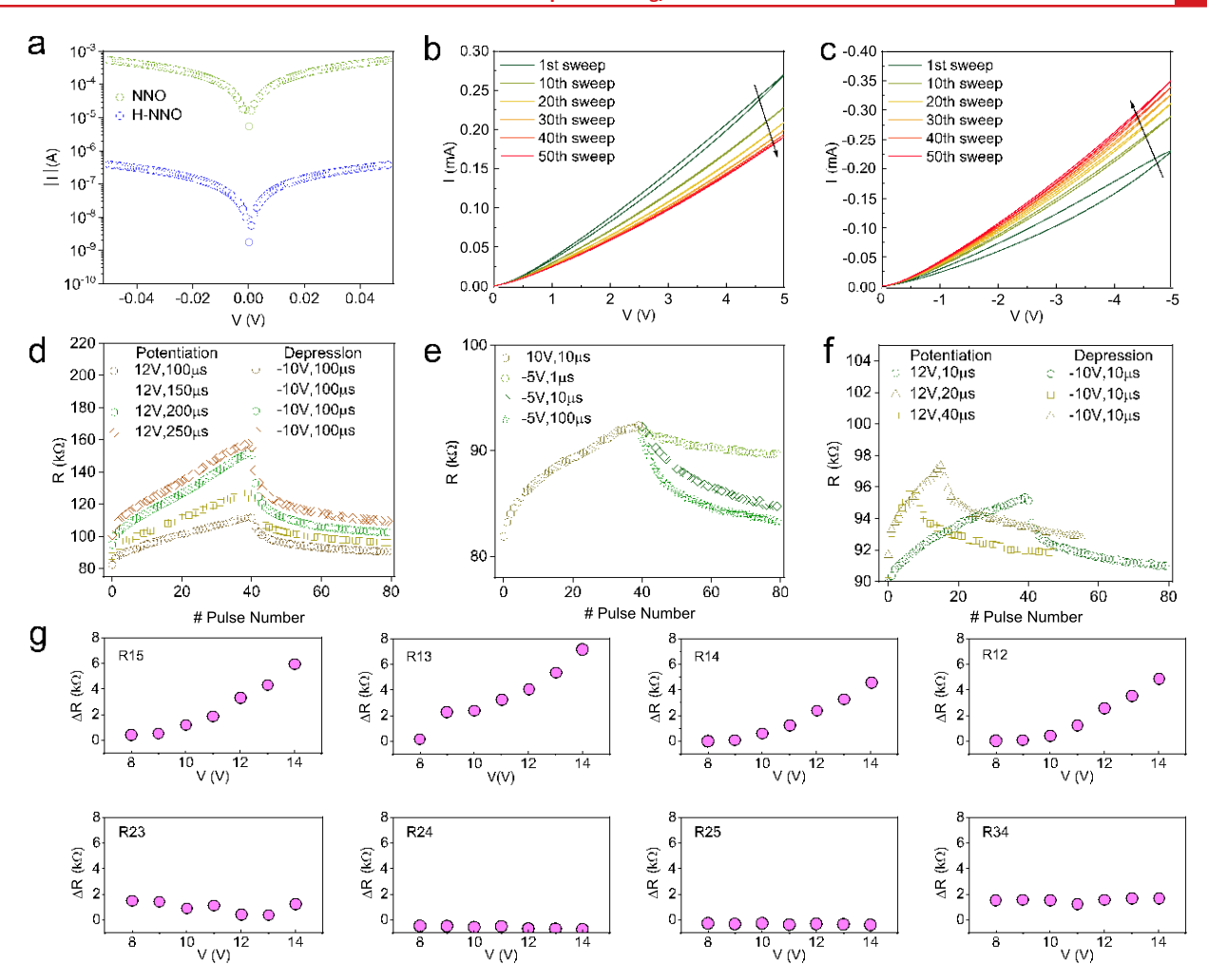


Figure 2. Demonstration of plasticity in H-NNO thin film device and the emergence of coupling and resistance evolution. (a) I-V characteristics of NNO and H-NNO films. A several-order-of-magnitude change in the resistance of H-NNO film compared to the NNO film indicates carrier localization upon electron doping. (b, c) I-V characteristics (shown for every 10th cycle) under a positive and negative voltage sweep show a continuous increase and decrease in the resistance of the H-NNO device, respectively. The modulation of device resistance depends on the spatial drift of interstitial protons in the presence of an electric field. (d) Potentiation and depression curves for the H-NNO device. Different stimuli were used for the potentiation while keeping the stimulus the same during the depression. Tuning the device resistance to different states by changing the stimuli for (e) depression and (f) potentiation. In both cases, a constant  $\Delta R$  was maintained. (g) An electric pulse E of varying magnitude and pulse width 100  $\mu$ s is applied across electrodes 1 and 5, and a change in resistance  $\Delta R = R - R$  across various pairs of electrodes is shown. The electric pulse modulates the proton distribution near electrode 1 and hence affects the resistance of adjacent electrodes (R12, R13, R14) in the vicinity of electrode 1. An increase in the R13 could likely be attributed due to a current flow from electrode 1 to electrode 5 and electrode 5 to electrode 3. Therefore, a combination of R15 and R35 might be responsible for a slightly larger effect than that of R15 or R12/R14.

electrical measurements). A significantly increased resistance for H-NNO in contrast to NNO film is attributed to the hydrogen doping that is controlled by the forming gas annealing conditions. The proton–electron doping in the NNO film leads to a large increase in the electronic bandgap due to carrier localization of the doubly occupied e manifold by reducing Ni<sup>3+</sup> sites to Ni<sup>2+</sup>, and therefore a significant change in overall device resistance can be observed. To understand the device response to the polarity of an electric field, the electric field sweeps (50 cycles) for an asymmetric H-NNO device are depicted in Figures 2b and 2c. As observed, the resistance of the device increases with the application of a positive field sweep while it decreases with a negative field sweep. The electric-field-driven modulation of resistance can be attributed due to the diffusion of interstitial protons in the

H-NNO lattice. This also suggests that application of positive bias results in the expansion of the H-NNO region due to proton migration, and vice versa. We then exploit this aspect to emulate the plasticity based on the H-NNO device, i.e., mimicking the potentiation and depression process. To elucidate the plasticity, continuous electric pulses of magnitude 12 V and pulse width 100  $\mu$ s were applied to increase the device resistance by nearly 25 k $\Omega$ , and the device resistance was then reduced to nearly the original state by applying electric pulses of -10 V and 100  $\mu$ s. Moreover, the rate of potentiation and depression can be tuned by the magnitude of electric pulses, as shown in Figure 2d. In Figures 2e and 2f, we also show that the device resistance can be modulated to multiple resistance states and can be tuned back to the original resistive state. The resistance tuning mechanisms follow a

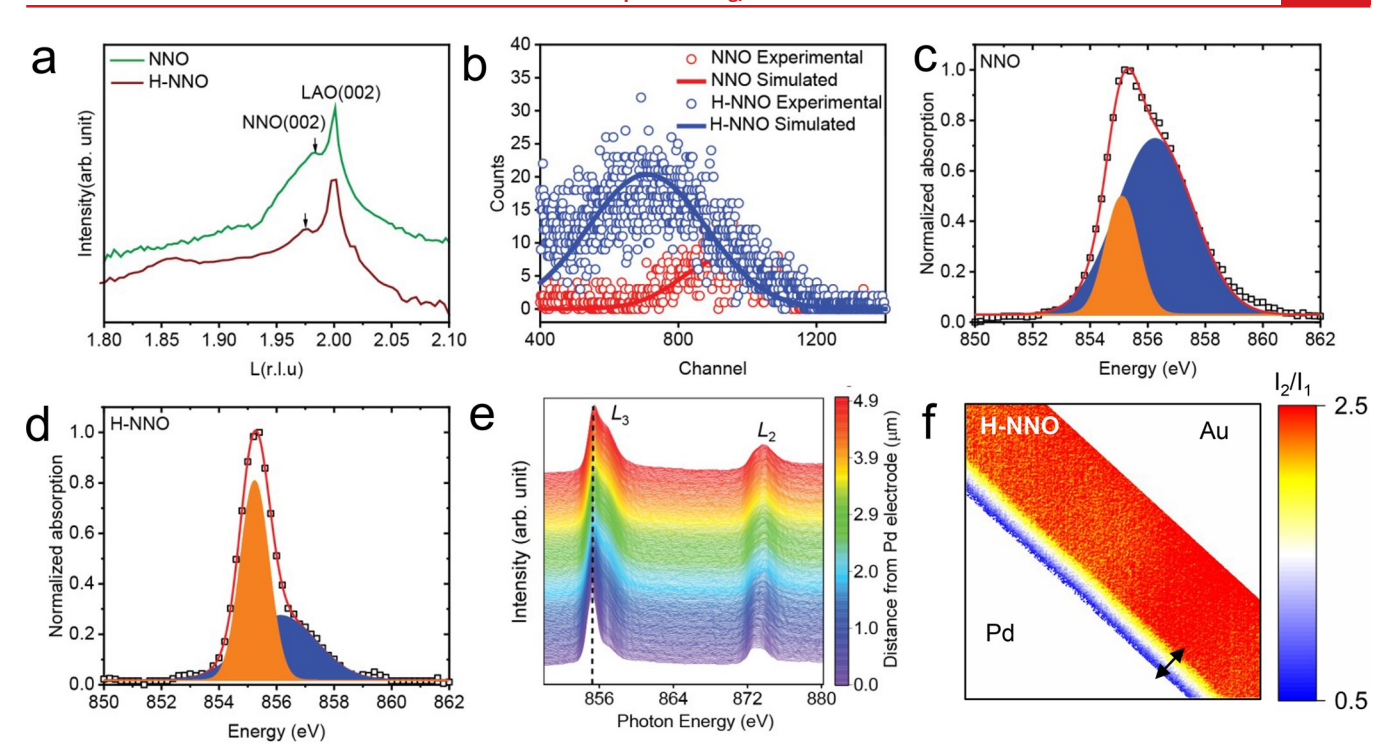


Figure 3. Structural and electronic structure characterization of H-NNO films. (a) Synchrotron micro XRD pattern of NNO and H-NNO films. The reciprocal lattice unit (r.l.u.) was defined using the lattice parameter (a 2 3.79 Å) of the LAO (001) substrate. The arrow marks the peak position of NNO before and after hydrogen doping. (b) ERDA analysis for pristine NNO and H-NNO film showing an increase in hydrogen content for H-NNO film. The solid lines in each curve represent the corresponding simulated spectrum. An offset in channel number for H-NNO is due to a Pt film on top used for hydrogenation. (c, d) Deconvoluted normalized XAS Ni L edge spectra of NNO and H-NNO films. (e) A full range XAS spectra of H-NNO film as a function of distance from the Pd edge. The dashed line marks the shift in peak positions. (f) Spatially resolved area ratio  $I_2/I_1$  of the Ni L<sub>3</sub> spectra of the H-NNO film. The arrow marks the width ( $22 \mu m$ ) of the doped region near the Pd electrode.

power law and are nonlinear;  $^{25-27}$  the nonlinearity factor increases with an increase in pulse width (Figure S2). Representative retention and endurance data are listed in Figure S3. The resistance switching mechanism for the H-NNO film describing the relationship between proton migration (that results in expansion of the H-NNO region) and resistance modulation has been proposed in the literature.  $^{20,28}$  Using Einstein's relation  $D = \mu K_B T/q$  and  $v_d = \mu E$ , the proton migration distance for the H-NNO device can be written as  $^{29}$ 

$$\Delta x = \frac{\Delta t q D V}{K_B T L}$$
, where  $v_d = \frac{\Delta x}{\Delta t}$ 

 $v_d$ ,  $\mu$ ,  $\Delta t$ , q, D, V,  $K_B$ , T, E, and L represent the drift velocity, proton mobility, pulse width of a single electric bias stimulus, charge, diffusion constant, pulse voltage, Boltzmann constant, temperature, electric field, and width of the channel, respectively. For  $\Delta t = 100~\mu s$ , V = 12~V, and  $L = 10~\mu m$  (one representative experimental condition used in our study), the estimated proton migration length is 20.40~m for a representative proton diffusion coeficient of  $8.7 \times 10^{-10}~cm^2/s$  (diffusion constant adapted from ref 20). It is likely the primary mechanism that modulates the resistance is the HNNO/NNO interface proton distribution (due to the growth of the H-NNO region upon positive bias) and is also noted from Kelvin force microscopy measurements of the electrode—HNNO interface before and after application of electric stimuli as described later.

The spatial concentration of the local hydrogen ion distribution in the H-NNO-based artificial synapse was

modulated systematically by applying varying electrical pulses across one device junction, and the resistance evolution across all the pairs of devices was studied. The optical image of the device studied is shown in Figure S1. Further, we demonstrate how this affects the properties of neighboring devices, as shown in Figure 2g. A single positive electrical pulse of varying magnitude  $(E_i)$  was applied across electrodes 1 and 5, and resistance evolution ( $\Delta R = R_f - R_i$ ) across other pairs of electrodes (R12, R13, R14 R15, R23, R24, R25, R34, R35, and R45) was measured. The  $R_i$  and  $R_f$  represent the initial resistance of the junction and the resistance of the junction after pulsing. As shown, the electrodes that are in the vicinity of electrode 1 show a monotonic increase in the resistance, a behavior similar to the R15. Importantly, this change in resistance or equivalent synaptic weight update for R12, R13, and R14 occurs without applying any additional electrical pulse across them. This increase in resistance at the adjacent junctions can be attributed to the change in the local proton distribution near electrode 1 upon electrical pulsing. The other pairs of devices (R23, R24, R25, R34, R35, and R45) do not show significant variation in the resistance. Figure S4 further presents modulation of junction resistance across various pairs when an electric pulse was applied between electrodes 2 and 5 establishing general validity.

To understand how plasticity and synaptic coupling in H-NNO film can be utilized for biologically inspired computation, we then investigated signal integration through various junctions (see Figure S5 and the Supporting Information). Signal integration operation is similar to a

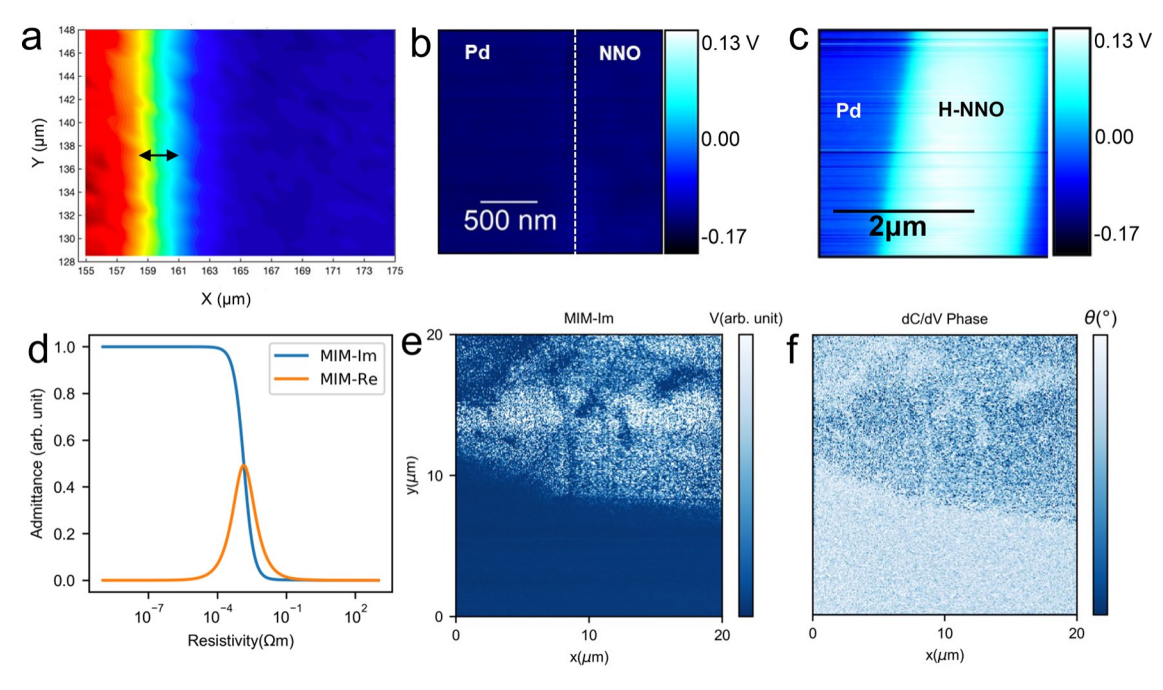


Figure 4. Spatial characterization of H-NNO films. (a) Microdiffraction 2D mapping of H-NNO film intensity (L=1.85) demonstrates the extended width of the hydrogen-doped region away from the edge of Pd. The arrow marks the width ( $\mathbb{Z}_2$   $\mu$ m) of the doped region. KPFM contact potential difference map of the asymmetric (b) NNO and (c) H-NNO device. The dashed line in (b) represents the boundary between the Pd electrode and the NNO film. A distinct difference in the contact potential difference profile for H-NNO device is attributed due to hydrogen doping. A contrast in the contact potential difference near the Pd electrode for H-NNO film represents the areal extent of the hydrogen doping. The estimated width of the doped region is in good agreement with the micro diffraction mapping, LEEM, and XPEEM imaging. (d) Theoretical MIM response curves, simulated using finite-element analysis at 155 MHz, show how the reflected MIM signal depends on the local resistivity of the sample. A small-area scan in the immediate vicinity of the boundary between the H-NNO and NNO areas. (e) The imaginary MIM channel and (f) the relative phase of the dC/dV mode image.

weighted sum operation, widely used in artificial neural networks. 30–33

To check the phase purity and structural evolution upon hydrogen doping in NNO film, the NNO and H-NNO films were characterized by synchrotron XRD using a microprobe (see the Supporting Information) as shown in Figure 3a. Because of a lattice mismatch between the film and substrate, the NNO film experiences an in-plane biaxial compressive 3.822 Å, is larger than its bulk value of 3.807 Å.<sup>21</sup> Moreover, upon hydrogen doping the NNO peak further shifts to the lower L values, and the out-of-plane lattice parameter ( $c_{
m NNO}$   $\ \ \, \ \ \, \ \ \,$ 3.836 Å) shows a further elongation by 20.4%. In Figures S6a and S6b, we also show the evolution of the doping profile between the Pd and Au electrodes for the device shown in Figure S1. As shown, the doping is dense near the Pd electrode and eventually fades toward the Au electrodes. The micro XRD pattern of NNO and H-NNO films hence reveals an oriented (002) single-phase film grown on a LaAlO<sub>3</sub> substrate.

To measure the elemental composition as well as hydrogen concentration in the nickelate films, we performed Rutherford backscattering spectroscopy (RBS) and elastic recoil detection analysis<sup>34</sup> (ERDA) (see the Supporting Information). Figure S7a,b shows the RBS analysis of the NNO and H-NNO films. The NNO films are highly stoichiometric (Table S1). ERDA shows a clear increase in the hydrogen concentration in the doped films versus the undoped ones (Figure 3b). The ratio of the spatially averaged areal density of hydrogen to nickel estimated from experiments is 0.14 (H/Ni ② 0.14), suggesting a partially doped H-NNO film. A similar increase in proton concentration (H/Ni ② 0.18) has also been verified for a

control sample independently prepared from electrochemically H-doped NNO film to verify the ERDA profile (Figure S8 and Table S2). The electronic structure of undoped and electrochemically doped films was also characterized using X-ray photoelectron spectroscopy XPS<sup>35</sup> (Figure S9) and indicates expected oxidation states and metallic vs semiconductor character (see the Supporting Information).

We then utilized nanoscale X-ray absorption spectroscopy (XAS) to understand the proton distribution and change in the electronic structure near the Pd and Au electrodes (see the Supporting Information). In Figures 3c and 3d, we show the XAS analysis of the Ni L<sub>3</sub> edges of the NNO and H-NNO films. The multiplets were deconvoluted after a baseline subtraction and the spectra were fitted with two Gaussian components assigned for high energy (2856.3 eV) and low energy (2855.2 eV) peaks. 36,37 As shown, the normalized integrated intensity for the low-energy peak  $(I_1)$  and highenergy peak  $(I_2)$  is enhanced (orange) and suppressed (blue) as a consequence of hydrogen doping and suggests a reduction in the Ni valence in H-NNO films near the Pd electrode. A full-range XAS scan of the Ni L  $_{\rm 2,3}$  edge for H-NNO film is depicted in Figure 3e. As shown, a clear shift in the spectral weight of the Ni L<sub>2,3</sub> edge to the lower energy, away from the Au electrode, is attributed to a reduced Ni valence because of hydrogen doping near the catalytic Pd electrode. To understand the spatial variation and elucidate the extent of hydrogen doping in H-NNO films, the spatially resolved analysis of area ratio  $I_2/I_1$  (Ni L<sub>2</sub> edge) was employed. It shows a heavily doped region of nearly 2  $\mu$ m close to the Pd electrode (Figure 3f). In Figure S10, we also plot  $I_2/I_1$  as a function of distance from the Pd electrode. The spectral weight evolution

of the low-energy peak toward the Pd electrode thus confirms the dominant presence of Ni<sup>2+</sup> near the Pd electrode. The spatially resolved XAS analysis thus suggests a mixture of majority H-NNO regions and minority NNO regions in a solid matrix near the Pd electrode. Moreover, toward the Au electrode, the H-NNO regions are the minority in the solid matrix. Modulating these granular regions with electrical pulsing redistributes the protons and may lead to observed electrical behavior (Figure 2g). Additionally, microdiffraction mapping, X-ray photoemission electron microscopy (XPEEM),<sup>38</sup> and low-energy electron microscopy (LEEM) (see the Supporting Information, Figure 4a, and Figure S11) shows a width of doped region consistent with the XAS study.

To understand the electronic phase transition upon hydrogen doping, we performed scanning Kelvin probe force microscopy (KPFM). In Figures 4b and 4c, we depict a spatial map of the measured contact potential difference ( $V_{\rm CPD}$ ) for the NNO and H-NNO films, respectively. The areal extent of hydrogen doping for the H-NNO film decays spatially due to the diffusive nature of doping (Figure S12). KPFM also shows a similar width of the doped region. Moreover, upon electrical pulsing, the Pd-NNO interface remains nearly unaffected while H-NNO/NNO shows changes (see the Supporting Information and Figures S13 and S14 showing KPFM data). This further suggests the mechanism of change in resistance upon electrical pulsing is primarily due to proton migration.

While the spectroscopy and microscopy techniques utilized above give detailed information on the electronic structure/ surface potential, a local conductivity map over a large region can provide additional evidence of the inhomogeneous doping, which leads to the phase coexistence of NNO and H-NNO regions in a solid matrix. To acquire a conductivity map, we employed microwave impedance microscopy (MIM) (see the Supporting Information and Figure S15) to image the conductivity contrast across the interface of the NNO and H-NNO region. The scan area, represented by the red box in Figure S16, encloses both the H-NNO and the pristine NNO regions. Our measurements reveal that local changes in conductivity are spatially correlated to the real-space distribution of hydrogen doping. The technique of MIM probes the electronic properties of materials by measuring the complex tip-sample admittance, which depends on the local permittivity and conductivity of the sample. The theoretical real and imaginary parts of the MIM response (MIM-Re and MIM-Im, respectively) are plotted in Figure 4d and obtained from finite element simulations of the experimental MIM setup at 155 MHz. At room temperature, prior experiments have reported that pristine NNO should have a resistivity of  $10^{-5} \Omega$ m.40 For comparison, the transport results reported in this work indicate that H-NNO should have a resistivity of nearly ☑10<sup>3</sup>–10<sup>4</sup> larger than the NNO. Therefore, based on the response curves in Figure 4d, it is expected that the resistive H-NNO region should yield a MIM-Im signal saturated near zero, while the conductive NNO region should have a finite MIM-Im signal that is saturated at the other end in the response curve. We should therefore see a clear MIM contrast between these two regions. The two panels (a) and (b) in Figure S17 display MIM-Im and MIM-Re images obtained near the boundary between the NNO and H-NNO regions, where the color change reflects the change in conductivity with the position. Right outside of the H-NNO region, nonuniform spatial features appear to penetrate from the H-NNO region

(Figure S17c). These spatial inhomogeneities of the local conductivity are more visible in the detailed scans of the interface shown in Figure 4e. Figures 4f and S17c display the relative phase of the dC/dV signal, which can shed light on the type of charge carrier. The H-NNO region shows a higher phase value relative to the pristine NNO region (Figure 4f), corresponding to the electrons that the hydrogen atoms donate.

In summary, multimodal spectroscopic characterization reveals that an electronically inhomogeneous nickelate medium due to graded hydrogen doping can serve as a platform for tuning electrical resistance upon voltage application. Future studies exploring different electrode geometries and network patterns could serve to examine the evolution of weights in more complex networks. Quantum materials whose electronic properties can be tuned by ion doping offer an interesting platform to examine neuromorphic functions.

# [

#### **ASSOCIATED CONTENT**

#### \* Supporting Information

The Supporting Information is available free of charge at https://pubs.acs.org/doi/10.1021/acs.nanolett.3c02076.

Details on experimental methods; weighted sum measurements; structural characterization of NNO thin films; optical image of the device used (Figure S1); nonlinearity analysis of potentiation and depression curves (Figure S2); device stability and electrical characterization of the H-NNO network (Figures S3 and S4); weighted sum measurements (Figure S5); detailed structural characterizations (Figures S6–S17, Tables S1 and S2) (PDF)



## AUTHOR

#### INFORMATION

**Corresponding Authors** 

Ravindra Singh Bisht – Department of Electrical and Computer Engineering, Rutgers University, Piscataway, New Jersey 08854, United States; orcid.org/0000-0002-8225-7306; Email: ravindra.bisht@rutgers.edu

Shriram Ramanathan – Department of Electrical and Computer Engineering, Rutgers University, Piscataway, New Jersey 08854, United States; Email: shriram.ramanathan@rutgers.edu

#### **Authors**

Jaeseoung Park – Department of Electrical and Computer Engineering, University of California, San Diego, La Jolla, California 92093, United States; orcid.org/0000-0002-7680-9709

Haoming Yu – School of Materials Engineering, Purdue University, West Lafayette, Indiana 47907, United States

Chen Wu – Department of Physics, University of California, San Diego, La Jolla, California 92093, United States

Nikhil Tilak – Department of Physics and Astronomy, Rutgers University, Piscataway, New Jersey 08854, United States

Sylvie Rangan – Department of Physics and Astronomy, Rutgers University, Piscataway, New Jersey 08854, United States; Occid.org/0000-0002-2367-5356

Tae J. Park – School of Materials Engineering, Purdue University, West Lafayette, Indiana 47907, United States; orcid.org/0000-0003-3810-1221

Nano Letters pubs.acs.org/NanoLett Letter

Yifan Yuan – Department of Electrical and Computer Engineering, Rutgers University, Piscataway, New Jersey 08854, United States

Sarmistha Das – Department of Physics, University of California, San Diego, La Jolla, California 92093, United States: © orcid.org/0000-0002-1744-6119

Uday Goteti - Department of Physics, University of California,

San Diego, La Jolla, California 92093, United States Hee Taek Yi – Department of Physics and Astronomy, Rutgers University, Piscataway, New Jersey 08854, United States;

orcid.org/0000-0002-8998-777 4

Hussein Hijazi – Department of Phy<sup>S</sup>ics and Astronomy, Rutgers University, Piscataway, New Jersey 08854, United

Abdullah Al-Mahboob – Center for Functional Nanomaterials, Brookhaven National Laboratory, Upton, New York 11973, United S btes

Jerzy T. Sadowski – Center for Functional Nanomaterials, Brookhaven National Laboratory, Upton, New York 11973, United States; o orcid.org/0000-0002-4365-7796

Hua Zhou – X-ray Science Division, Advanced Photon Source, Argonne National Laboratory, Lemont, Illinois 60439, United States; oorcid.org/0000-0001-9642-8674

Seongshik Oh – Department of Physics and Astronomy, Rutgers University, Piscataway, New Jersey 08854, United States; oorcid.org/0000-0003-1681-516X

Eva Y. Andrei – Department of Physics and Astronomy, Rutgers University, Piscataway, New Jersey 08854, United States

Monica T. Allen – Department of Physics, University of California, San Diego, La Jolla, California 92093, United States; orcid.org/0000-0002-7992-6951

Duygu Kuzum – Department of Electrical and Computer Engineering, University of California, San Diego, La Jolla, California 92093, United States

Alex Frano – Department of Physics, University of California, San Diego, La Jolla, California 92093, United States

Robert C. Dynes – Department of Physics, University of California, San Diego, La Jolla, California 92093, United States

Complete contact information is available at: https://pubs.acs.org/10.1021/acs.nanolett.3c02076

#### **Author Contributions**

R.S.B., J.P., D.K., A.F., R.C.D., and S.R. designed the study. R.S.B., J.P., H.Y., C.W., N.T., S.R., and S.D. performed the research; R.S.B. and H.Y. grew the samples and fabricated the devices. R.S.B. and J.P. performed electrical measurements. S.R. performed XPS and valence band measurements. R.S.B. and H.T.Y. performed catalytic hydrogen doping using a furnace setup by S.O. T.J.P. performed hydrogen doping electrochemically. C.W. and M.T.A. performed MIM measurements. H.H. performed RBS and ERDA measurements. N.T. and R.S.B. performed KPFM measurements and analysis. H.Z. performed synchrotron micro XRD measurements. A.M. and J.S. performed XAS, XPEEM, and LEEM measurements. R.S.B. and J.P. analyzed the data. R.S.B., J.P., D.K., and S.R. wrote the paper with input from all the authors. All the authors discussed the results.

#### Notes

The authors declare no competing financial interest.

## **ACKNOWLEDGMENTS**

The network concept development and electrical measurements supported as part of the Quantum Materials for Energy Eficient Neuromorphic Computing (Q-MEEN-C), an Energy Frontier Research Center funded by the U.S. Department of Energy (DOE), Ofice of Science, Basic Energy Sciences (BES), under Award # DE SC0019 273. T his rese arch used resources of the Center for Functional Nanomaterials and the National Synchrotron Light Source II, which are U.S. Department of Energy (DOE) Ofice of Science facilities at Brookhaven National Laboratory, under Contract DE-SC0012704. Thi s research used resources of the Advanced Photon Source, a U.S. Department of Energy (DOE) Ofice of Science user facility at Argonne National Laboratory, and is based on res arch supported by the U.S. DOE Ofice of Science-Basic Energy Sciences, under Contract DE-AC02-06CH11357. We acknowledge AFOSR Grant FA9550-22-1-0344 that supported the ion beam scattering characterization of the films. H.T.Y. and S.O. are supported by National Science Foundation's DMR2004125 and the Center for Quantum Materials Synthesis (cQMS), funded by the Gordon and Betty Moore Foundation's EPiQS initiative through Grant GBMF10104. The authors acknowledge the Laboratory for Surface Modification Facilities at Rutgers University for XPS, ERDA, and RBS measurement<sup>S</sup>. N.T. and E.Y.A. acknowledge Gordon and Betty Moore Foundation EPiQS initiative GBMF9453 and Department of Energy DOE-FG02-99ER45742 for support. R.S.B., Y.Y., and S.R. gratefully thank Kevin Wine at Rutgers University for helping set up the probe station. R.S.B. and S.R. thank Professor Leonard C. Feldman from Rutgers University for an insightful discussion on ion beam analysis. S.R. thanks Professor Alberto E. Pereda from the Albert Einstein College of Medicine for valuable discussions on synapses in teleost fish.

# ? REFERENCES

- (1) Abbott, L. F.; Nelson, S. B. Synaptic plasticity: taming the beast. *Nat. Neurosci.* 2000, *3*, 1178–1183.
- (2) Alcamí, P.; Pereda, A. E. Beyond plasticity: the dynamic impact of electrical synapses on neural circuits. *Nat. Rev. Neurosci.* 2019, *20*, 253–271.
- (3) Abbott, L. F.; Regehr, W. G. Synaptic computation. *Nature* 2004, 431, 796–803.
- (4) Pereda, A. E. Electrical synapses and their functional interactions with chemical synapses. *Nat. Rev. Neurosci.* 2014, *15*, 250–263.
- (5) Faber, D. S.; Pereda, A. E. Two forms of electrical transmission between neurons. *Front. Mol. Neurosci.* 2018, *11*, 427.
- (6) Traub, R. D.; Kopell, N.; Bibbig, A.; Buhl, E. H.; LeBeau, F. E.; Whittington, M. A. Gap junctions between interneuron dendrites can enhance synchrony of gamma oscillations in distributed networks. *J. Neurosci.* 2001, *21* (23), 9478–86.
- (7) Pernelle, G.; Nicola, W.; Clopath, C. Gap junction plasticity as a mechanism to regulate network-wide oscillations. *PLoS Comput. Biol.* 2018, *14* (3), No. e1006025.
- (8) Traub, R. D.; Schmitz, D.; Jefferys, J. G.; Draguhn, A. High-frequency population oscillations are predicted to occur in hippocampal pyramidal neuronal networks interconnected by axoaxonal gap junctions. *Neurosci.* 1999, *92* (2), 407–26.
- (9) LeBea<sup>U</sup>, F. E.; Traub, R. D.; Monyer, H.; Whittington, M. A.; Buhl, E. H. The role of electrical signaling via gap junctions in the generation of fast network oscillations. *Brain Res. Bull.* 2003, *62* (1), 3–13.
- (10) Bragin, A.; Engel, J., Jr.; Wilson, C. L.; Fried, I.; Buzsáki, G. High-frequency oscillations in human brain. *Hippocampus*. 1999, *9* (2), 137–42.

Nano Letters pubs.acs.org/NanoLett Letter

- (11) Buzsaki, G.; Draguhn, A. Neuronal oscillations in cortical networks. *Science*. 2004, *304* (5679), 1926–1929.
- (12) Canakci, S.; Toy, M. F.; Inci, A. F.; Liu, X.; Kuzum, D. Computational analysis of network activity and spatial reach of sharp wave-ripples. *PLoS One* 2017, *12* (9), No. e0184542.
- (13) Buzsaki, G. Rhythms of the Brain; Oxford University Press: Oxford, 2006.
- (14) Hopfield, J. J. Neural networks and physical systems with emergent collective computational abilities. *Proc. Natl. Acad. Sci. U. S. A.* 1982, *79*, 2554–2558.
- (15) Amit, D. J.; Gutfreund, H.; Sompolinsky, H. Spin-glass models of neural networks. *Phys. Rev. A* 1985, *32*, 1007.
- (16) Peretto, P. Collective properties of neural networks: a statistical physics approach. *Biol. Cybern.* 1984, *50*, 51–62.
- (17) Goteti, U. S.; Zaluzhnyy, I. A.; Ramanathan, S.; Dynes, R. C.; Frano, A. Low-temperature emergent neuromorphic networks with correlated oxide devices. *Proc. Natl. Acad. Sci. U. S. A.* 2021, *118*, 35.
- (18) Shi, J.; Zhou, Y.; Ramanathan, S. Colossal resistance switching and band gap modulation in a perovskite nickelate by electron doping. *Nat. Commun.* 2014, *5*, 1–9.
- (19) Oh, C.; Heo, S.; Jang, H. M.; Son, J. Correlated memory resistor in epitaxial NdNiO<sub>3</sub> heterostructures with asymmetrical proton concentration. *Appl. Phys. Lett.* 2016, *108*, 122106.
- (20) Sidik, U.; Hattori, A. N.; Rakshit, R.; Ramanathan, S.; Tanaka, H. Catalytic hydrogen doping of NdNiO<sub>3</sub> thin films under electric fields. *ACS Appl. Mater. Interfaces.* 2020, *12* (49), 54955–54962.
- (21) Catalan, G. Progress in perovskite nickelate research. *Phase Transit*. 2008, 81, 729–749.
- (22) Catalano, S.; Gibert, M.; Fowlie, J.; Iniguez, J.; Triscone, J.- M.; Kreisel, J. Rare-earth nickelates RNiO<sub>3</sub>: thin films and heterostructures. *Rep. Prog. Phys.* 2018, *81*, No. 046501.
- (23) Middey, S.; Chakhalian, J.; Mahadevan, P.; Freeland, J. W.; Millis, A. J.; Sarma, D. D. Physics of ultrathin films and heterostructures of rare-earth nickelates. *Annu. Rev. Mater. Res.* 2016, *46*, 305–334.
- (24) Zhou, Y.; Guan, X.; Zhou, H.; Ramadoss, K.; Adam, S.; Liu, H.; Lee, S.; Shi, J.; Tsuchiya, M.; Fong, D. D.; Ramanathan, S. Strongly correlated perovskite fuel cells. *Nature* 2016, *534*, 231–234.
- (25) Tang, J.; He, C.; Tang, J.; Yue, K.; Zhang, Q.; Liu, Y.; Wang, Q.; Wang, S.; Li, N.; Shen, C.; Zhao, Y.; et al. A reliable all-2D materials artificial synapse for high energy-efficient neuromorphic computing. *Adv. Funct. Mater.* 2021, *31*, 2011083.
- (26) Chen, P. Y.; Lin, B.; Wang, I. T.; Hou, T. H.; Ye, J.; Vrudhula, S.; Seo, J. S.; Cao, Y.; Yu, S. Mitigating effects of non-ideal synaptic device characteristics for on-chip learning. *IEEE/ACM International Conference on Computer-Aided Design (ICCAD)*, 2015; pp 194–199.
- (27) Tang, J.; Bishop, D.; Kim, S.; Copel, M.; Gokmen, T.; Todorov, T.; Shin, S.; Lee, K. T.; Solomon, P.; Chan, K.; Haensch, W. ECRAM as scalable synaptic cell for high-speed, low-power neuromorphic computing. *IEEE International Electron Devices Meeting (IEDM)*. 2018, 13–1
- (28) Sidik, U.; Hattori, A. N.; Hattori, K.; Alaydrus, M.; Hamada, I.; Pamasi, L. N.; Tanaka, H. *ACS Appl. Electron. Mater.* 2022, *4* (10), 4849–4856.
- (29) Sidik, U.; Hattori, A. N.; Li, H. B.; Nonaka, S.; Osaka, A. I.; Tanaka, H. *Appl. Phys. Express.* 2023, *16*, No. 014001.
- (30) He, K.; Zhang, X.; Ren, S.; Sun, J. Deep Residual Learning for Image Recognition. *Proceedings of the IEEE Conference on Computer Vision and Pattern Recognition*. 2016, 770–778.
- (31) Krizhevsky, A.; Sutskever, I.; Hinton, G. E. Imagenet classification with deep convolutional neural networks. *Commun. ACM* 2017, *60*, 84–90.
- (32) Vaswani, A.; Shazeer, N.; Parmar, N.; Uszkoreit, J.; Jones, L.; Gomez, A. N.; Kaiser, Ł.; Polosukhin, I. Attention is all you need. *Advances in Neural Information Processing Systems* 2017, 30.
- (33) Oh, S.; Shi, Y.; Del Valle, J.; Salev, P.; Lu, Y.; Huang, Z.; Kalcheim, Y.; Schuller, I. K.; Kuzum, D. Energy-efficient Mott activation neuron for full-hardware implementation of neural networks. *Nat. Nanotechnol.* 2021, *16*, 680–687.

- (34) Feldman, L. C.; Mayer, J. W. Fundamentals of Surface and Thin Film Analysis; North-Holland: New York, 1986.
- (35) Amarasinghe, D. K.; Yu, H.; Rodolakis, F.; Zhou, H.; Cao, H.; Ramanathan, S. Electron doping of NdNiO<sub>3</sub> thin films using dual chamber CaH, annealing. *J. Solid State Chem.* 2022, *315*, 123512.
- (36) Medarde, M.; Fontaine, A.; García-Munoz, J. L.; Rodríguez-Carvajal, J.; De Santis, M.; Sacchi, M.; Rossi, G.; Lacorre, P. RNiO <sub>3</sub> perovskites (R= Pr, Nd): Nickel valence and the metal-insulator transition investigated by x-ray-absorption spectroscopy. *Phys. Rev. B* 1992, *46*, 14975.
- (37) Freeland, J. W.; van Veenendaal, M.; Chakhalian, J. Evolution of electronic structure across the rare-earth RNiO <sub>3</sub> series. *J. Electron Spectrosc. Relat. Phenom.* 2016, 208, 56–62.
- (38) Li, J.; Green, R. J.; Zhang, Z.; Sutarto, R.; Sadowski, J. T.; Zhu, Z.; Zhang, G.; Zhou, D.; Sun, Y.; He, F.; Ramanathan, S.; Comin, R. Sudden collapse of magnetic order in oxygen-deficient nickelate films. *Phys. Rev. Lett.* 2021, *126*, 187602.
- (39) Melitz, W.; Shen, J.; Kummel, A. C.; Lee, S. Kelvin probe force microscopy and its application. *Surf. Sci. Rep.* 2011, *66*, 1–27.
- (40) Preziosi, D.; Lopez-Mir, L.; Li, X.; Cornelissen, T.; Lee, J. H.; Trier, F.; Bouzehouane, K.; Valencia, S.; Gloter, A.; Barthélémy, A.; Bibes, M. Direct mapping of phase separation across the metalisulator transition of NdNiO<sub>2</sub>. *Nano Lett.* 2018, *18*, 2226.
- (41) Kundhikanjana, W.; Yang, Y.; Tanga, Q.; Zhang, K.; Lai, K.; Ma, Y.; Kelly, M. A.; Li, X. X.; Shen, Z. X. Unexpected surface implanted layer in static random access memory devices observed by microwave impedance microscope. *Semicond. Sci. Technol.* 2013, *28*, No. 025010.